

**Distributions of deposits and hydrogen on the upper and lower TDUs3 target
elements of Wendelstein 7-X**

Mingzhong Zhao^{1,*}, S. Masuzaki^{1,2}, G. Motojima^{1,2}, M. Tokitani^{1,2}, M. Yajima^{1,2}, Y. Gao³, M. Jakubowski³, A. Puig. Sitjes³, F. Pisano⁴, C.P. Dhard³, D. Naujoks³, J. Romazanov⁵, S. Brezinsek⁵ and the W7-X team⁶

¹National Institute for Fusion Science, National Institutes of Natural Sciences, Toki, 509-5292, Japan

²Graduate University for Advanced Studies, SOKENDAI, Toki, 509-5292, Japan

³Max-Planck-Institut für Plasmaphysik, 17491 Greifswald, Germany

⁴Department of Electrical and Electronic Engineering, University of Cagliari, Cagliari, Italy

⁵Forschungszentrum Jülich, Institut für Energie- und Klimaforschung—Plasmaphysik, Partner of the Trilateral Euregio Cluster (TEC), 52425 Jülich, Germany

⁶The W7-X team are the co-authors mentioned in the paper, Thomas Sunn Pedersen et al, 2022 Nucl. Fusion 62 042022, <https://doi.org/10.1088/1741-4326/ac2cf5>

Corresponding author.

E-mail address: zhao.mingzhong@nifs.ac.jp

Abstract

Distributions of deposits and hydrogen (H) on the graphite divertor target elements TM4h4 and TM3v5 in the test divertor units 3 (TDUs3) of Wendelstein 7-X (W7-X) are studied. The TM4h4 and TM3v5 are located at the magnetically symmetric positions in the upper and lower divertor. The microstructure of the deposition layer is characterized by a transmission electron microscope (TEM) combined with a focused ion beam (FIB). Metallic deposits such as iron (Fe), molybdenum (Mo), chromium (Cr) are detected in the deposition layer by energy-dispersive X-ray spectroscopy (EDS). The depth-resolved distribution patterns of boron (B) and metallic deposits on upper and lower horizontal (h) divertor target elements TDUs3-TM4h4 as well as upper and lower vertical (v) divertor target elements TDUs3-TM3v5 are clarified by glow discharge optical emission spectrometry (GDOES). Results for both TDUs3-TM4h4 and TDUs3-TM3v5 show that the B deposition regions exhibit higher H retention due to the co-deposition with deposits. On the other hand, up-down asymmetries in B deposition caused by particle drift exist on both TDUs3-TM4h4 and TDUs3-TM3v5. The B deposition amount on upper TDUs3-TM4h4 is 40% smaller than that on lower TDUs3-TM4h4. While for the vertical target elements, the B deposition amount on upper TDUs3-TM3v5 is 35% larger than that on lower TDUs3-TM3v5. Meanwhile, a shift of around 3 cm in B deposition peaks is observed on upper and lower TDUs3-TM4h4 and TDUs3-TM3v5. Results of numerical simulation of carbon deposition/erosion profiles on the target elements using ERO2.0 code and power flux measured by infrared cameras are shown and compared with the above mentioned B profiles.

Key words: Distribution pattern of deposits, hydrogen retention, up-down asymmetry, Wendelstein 7-X

1. Introduction

Wendelstein 7-X (W7-X) aims to demonstrate continuous plasma operation in a stellarator. Understandings of the erosion of plasma facing components (PFCs) and the deposition layer formation on these PFCs are important to assess the capability of continuous operation from the view of components lifetime and material transport.

W7-X completed the island divertor operation using test divertor units (TDUs) in operation phase 1.2a (OP. 1.2a) and OP 1.2b [1]. These inertially cooled TDUs are distributed along the helical edge of the plasma contour and alternatively located on the upper and lower side of plasma in the five nearly identical modules (see Fig. 1 of Ref. [2]). Each TDU consists of 9 horizontal (h) and 3 vertical (v) target modules (TM). After OP 1.2b, substantial PFCs were extracted from the vacuum vessel for studying the plasma surface interactions (PSI) in the three-dimensional (3D) configuration fusion device. To date, the global distributions of deposits on the plasma facing wall after OP. 1.2a and OP. 1.2b were clarified by the colorimetry using a compact color analyzer [3]. The erosion and deposition of carbon (C) at the divertor were studied by the target elements with dedicated C/Mo (molybdenum) marker layer coatings [4–7] and ^{13}C tracer [8]. The strong erosion region on the target elements was observed at the strike line location. The erosion of target elements in OP 1.2b was suppressed by the reduction of light impurities such as oxygen in plasma by the application of boronization [9,10]. Based on the deposition pattern of ^{13}C on the target element, deposition was found mainly located at both sides of the strike line [8]. On the other hand, the up-down asymmetries in power load and strike line location on divertor were observed under standard configuration [11], low iota configuration [2,12], and high mirror configuration [13]. However, the deposits layer and the retention of hydrogen (H) on standard graphite divertor target elements as well as the up-down distribution of deposits have only been partially assessed so far [4,9] and further systematic studies are required.

In this study, post-mortem analyses were performed for the graphite vertical divertor target elements TM3v5 and horizontal divertor target elements TM4h4 from the upper (u) and lower (l) TDUs in module 3 (TDUs3u and TDUs3l). Microstructure and composition of deposition layer on target elements were characterized by transmission electron microscope (TEM) and energy dispersive X-ray spectroscopy (EDS) combined with a focused ion beam (FIB). The distribution of deposits and H retention on these target elements were clarified by glow discharge optical emission spectrometry (GDOES). Results of carbon (C) deposition/erosion on the target elements simulated by ERO2.0 code [9] and power flux measured by infrared cameras are shown to compare with the observed B distribution.

2. Experimental

Four divertor target elements i.e. TDUs3u-TM4h4, TDUs3l-TM4h4, TDUs3u-TM3v5 and TDUs3l-TM3v5 were analyzed in this study. Schematic positions of the analyzed target elements at a TDU are shown in Fig. 1. The target elements TM4h4 and TM3v5 are at a similar toroidal position in the upper and lower TDUs, which is a benefit for studying the up-down distribution of deposits on these target elements. These target elements experienced the plasma exposures during OP 1.2a and OP 1.2b campaigns of W7-X. The total discharge number and time in OP 1.2a and OP 1.2b for different magnetic configurations, namely standard configuration, high iota configuration, high mirror configuration and low iota configuration, are summarized in Table. 1 [4,14]. Likewise, the vacuum field line diffusion modelling simulated heat flux distribution on a TDU under various configurations can be found in Fig. 3 in Ref. [14]. The target elements were cut into small samples to fit into the experimental set-up for the measurements. As shown in Fig. 2, the horizontal and vertical target elements were cut along the slit between target elements and the yellow dash line which depicts the midline of target elements. The thickness of each small sample was reduced to 3 mm by cutting the samples. The samples A1-A23 of horizontal target elements and A1-A15 of vertical target elements were analyzed by GDOES.

The sample A-4 from TDUs3u-TM4h4, which located at the deposition dominant region, was analyzed by TEM. The TEM observation site was marked by a yellow dot on sample A-4, as shown in Fig. 2(a). The microstructure and chemical composition of deposition layer on the sample A-4 from TDUs3u-TM4h4 were characterized by using a TEM (JEM-2800, JEOL) equipped with an EDS. The TEM sample was fabricated by a FIB-scanning electron microscope (SEM) (nanoDUE'T NB5000, Hitach High-Tech). To protect the sample surface from the gallium (Ga) ion beam in the FIB, the surface of analyzed region was coated with C and tungsten (W) protective films.

A commercial GDOES (GDA750, Rigaku) was used to measure the depth profiles of deposits and H on the target elements. In the GDOES measurement, the sample was pressed on a silicon O-ring by airtight and then sealed the copper (Cu) anode. A Cu anode with an inner diameter of 2.5 mm was used in the measurement. The analyzed sample was sputtered by a radio frequency (RF) glow discharge using argon (Ar) gas with the following conditions: a constant current 62 mA and Ar working pressure 280 Pa. The emission intensities for measured elements were recorded as a function of sputtering time. The emission lines used for the measurement elements were H 121.567 nm, C 156.144 nm, boron (B) 249.773 nm, iron (Fe) 385.991 nm, molybdenum (Mo) 386.41 nm, chromium (Cr) 425.433 nm, nickel (Ni) 341.447 nm. The depth of sputtering crater was thereafter measured by a laser microscope, Kevence VK-X1000 series. The emission intensity as a function of time was finally converted to be mass concentration as a function of depth according to the standard ISO 16962 [15]. Standard deviations 6.7%, 38%, 4.3%, 0.45%, 34% and 14% were considered in the calibration results for B, Fe, Mo, C, Cr and Ni, respectively. Number of the GDOES measurement spots were 61 for horizontal target elements and 43 for vertical target elements, as depicted by the red dots in Fig. 2(a) and (b). There are left, right and middle GDOES measurement spots on each sample (except few samples on both sides or one side) and their centers are 5 mm to the left of sample, 5 mm to the right of sample and middle in horizontal direction of sample as shown in Fig. 2(c). In the vertical direction, the GDOES measurement spots locate at the vertical center of sample.

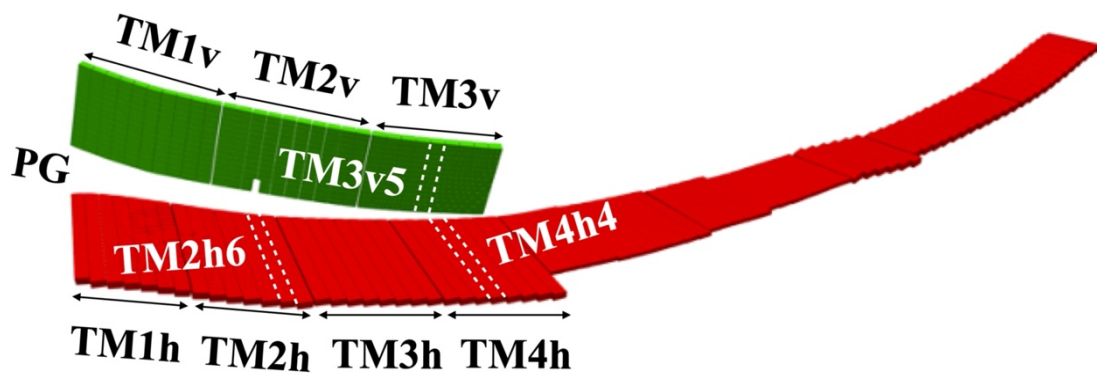


Fig. 1. Positions of analyzed target elements TM4h4 and TM3v5 at a TDU. Pumping gap (PG) is between the vertical divertor target and horizontal divertor target. TM2h6 on TDUs3 is the target element with C/Mo marker layer coating.

Table1. The combined number of plasma discharges and accumulated plasma duration in OP 1.2a and OP 1.2b for four magnetic configurations. For discharges in OP 1.2a, a discharge is defined by a diamagnetic energy (W_{dia}) above 50 kJ or ECRH power above 0.1 MW if W_{dia} is not available [4].

Configuration	Number of discharges	Plasma duration
Standard	1295	7290 s
High iota	459	2107 s
High mirror	591	2106 s
Low iota	169	1180 s

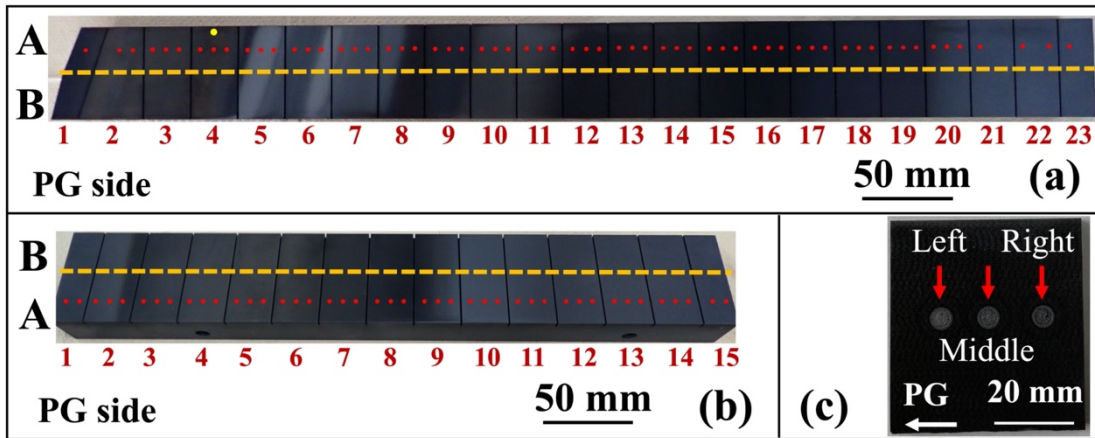


Fig. 2. Pictures of TDUs3u-TM4h4 (a) and TDUs3u-TM3v5 (b). PG shows the pumping gap side. A, B and number are the sample serial number. The yellow dash lines and red dots denote the cutting direction and positions of GDOES measurement. (c) Positions of GDOES measurement spots on one sample.

3. Results and discussion

3.1 Microstructure of deposition layer

The cross-section microstructure of deposition layer on the sample A-4 from TDUs3u-TM4h4 is shown in Fig. 3(a) which consists of 7 TEM images with overlapped boundaries. The boundary between deposition layer and divertor C matrix is depicted by the yellow dash line in Fig. 3(a). Likewise, the boundary between deposition layer and C protective layer is depicted by the red line in Fig. 3(a). The SEM image (Fig. 3(b)), in which a yellow arrow points the FIB cutting position, shows a rough surface on the A-4 sample. As shown in Fig. 3(a), a relatively thick deposition layer is formed in the valley while very thin layer on the hill. The thickness of deposition layer varies between 32~320 nm in the length of $\sim 4 \mu\text{m}$ which is the horizontal distance from left to right sides of the yellow dash line. Fig. 3(c) shows the EDS mapping results for the region depicted as a red dot frame in Fig. 3(a). The brighter contrast areas in EDS mapping images show the spatial distribution of corresponding elements. In the EDS mapping result for C, the bright contrast area on the top surface is the coated C protective layer. Metals such as Fe, Mo, Cr, are detected in the deposition layer. These metals were from the stainless steel (SUS) wall [14]. The erosion of C/Mo coated target elements during discharge can also contribute to the Mo deposition. The locations of C/Mo coated target elements in W7-X can be found in Ref. [4]. The C/Mo coated target elements, TM2h6, is located at the same divertor unit with the analyzed target elements, as shown in Fig. 1. Since EDS has a relatively poor resolution to B, the spatial distribution of B is not as clear as C, Fe, Mo and Cr in Fig. 3(c).

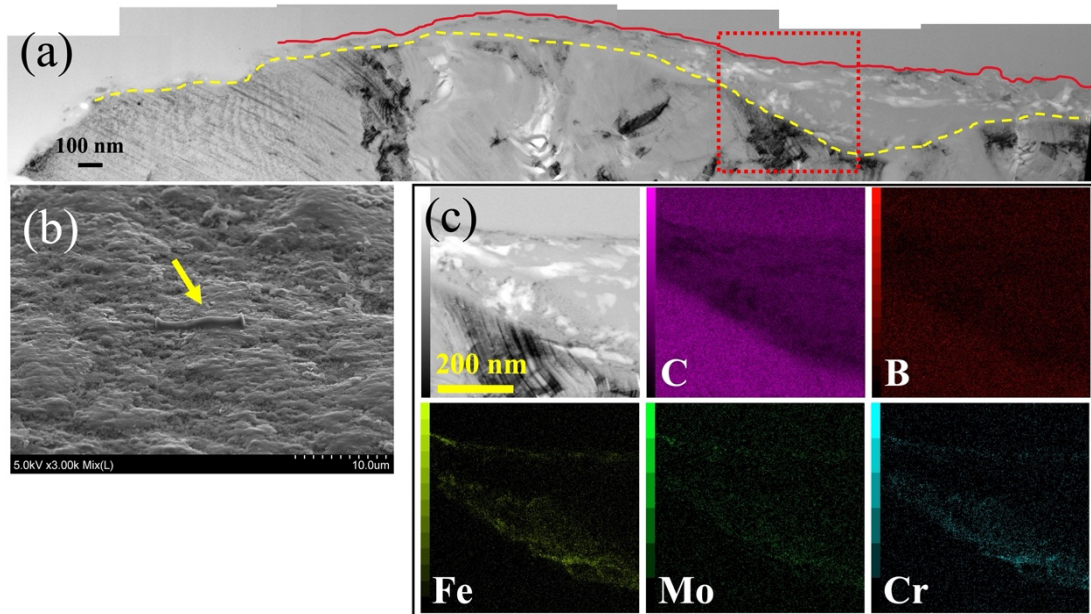


Fig. 3. Microstructure and composition of deposition layer on sample A-4 from TDUs3u-TM4h4. (a) The microstructure view (by TEM) of the cross-section of FIB cut. The yellow dash line indicates the boundary between deposition layer and divertor C matrix. The red line indicates the boundary between deposition layer and C protective layer. (b) Surface morphology (by SEM) of the sample surface around the FIB cut. The yellow arrow denotes the position of FIB cut. (c) EDS mapping of the area marked by a red dot frame in TEM image (a), showing the presence of difference elements.

3.2 Distribution patterns of deposits on target elements

The depth resolved distribution patterns of deposits on target elements are determined by GDOES. The diameter of GDOES measurement spot is 2.5 mm which is larger than the surface roughness of few microns, as observed by TEM (Fig. 3(a)). Therefore, the GDOES measurement shows a kind of average behavior over the spot. Based on the EDS results shown in Fig. 3(c), B, Fe, Mo, Cr, Ni, C are considered in the GDOES measurement. And the mass concentration of C, B, Fe, Mo, Cr, Ni are normalized to 100% in the GDOES results. Fig. 4(a), (b) and (c) show depth profiles of composition of deposition layers as well as the H intensity as a function of sputtering time at the middle measurement spots on samples A-8, A-9 and 9

A-20 from TDUs31-TM4h4. These samples were located at the erosion dominant, deposition dominant and low PSI regions, respectively. The concentration of Cr and Ni is not shown in Fig. 4 because their amounts are much smaller than others. The small peaks of B concentration in Fig. 4(b) are related to the boronization history of W7-X. Three boronizations by means of glow discharge with 10% B₂H₆+90% He mixture gas were applied in OP 1.2b which totally introduced 17.86 g B [16]. Furthermore, an in-situ B₄C powder injection was performed before the third boronization by the probe mounted particle injector (PMPI) [17]. The amount of injected B by PMPI was 1.57 g [16]. According to Fig. 4(d) which is an enlargement of Fig. 4(c), B also exists on the surface of low PSI region.

To obtain the overall distribution patterns of deposits on target elements, all of the GDOES results are plotted as a contour mapping. Photos of target elements, the depth resolved distribution patterns of B, Fe, Mo as well as H retention are shown in Fig. 5 for TDUs3-TM4h4 and Fig. 6 for TDUs3-TM3v5. Since H is not calibrated, the H retention behavior in target element is qualitatively analyzed by integrating H intensity over sputtering time. In the contour mapping, the X axis, Y axis and the color scale correspond to the poloidal coordinate (s), depth and mass concentration of element, respectively. The white vertical lines indicate the gap on target element which has a width of 0.8 mm. The side of target element towards the pumping gap (PG), which provides for the neutral particle exhaust, is set as the origin of the poloidal coordinate. It should be noted that the depth here is based on the surface height after experiencing the PSI processes in OP 1.2.

Fig. 5(a) and (b) show that two relatively large B deposition regions exist on both of TDUs3u-TM4h4 and TDUs31-TM4h4. The large B deposition region closes to the PG on TDUs3u-TM4h4 is thinner than that on the TDUs31-TM4h4. The region between the two large B deposition regions is the strike zone which corresponds to a white stripe as marked by yellow dot lines in the photos of the target elements. There is a continuous small B deposition region where $s = 222-402$ mm on TDUs3u-TM4h4. In the case of TDUs31-TM4h4, the continuous small B deposition region locates at $s = 253-409$ mm. Regions at $s > 402$ mm for TDUs3u-TM4h4 and $s > 409$ mm for

TDUs31-TM4h4 are the low PSI regions. The maximum B concentration is located under the surface, as shown in Fig. 5(b). This could be due to the gradual decrease of B deposition layer in the erosion region. It was turned out that B layer formed by boronization can sustain for about 200 plasma seconds at the strike line position of divertor [18]. The C matrix at the erosion dominant region is sputtered and transport to the deposition dominant region after the B layer is eroded by plasma.

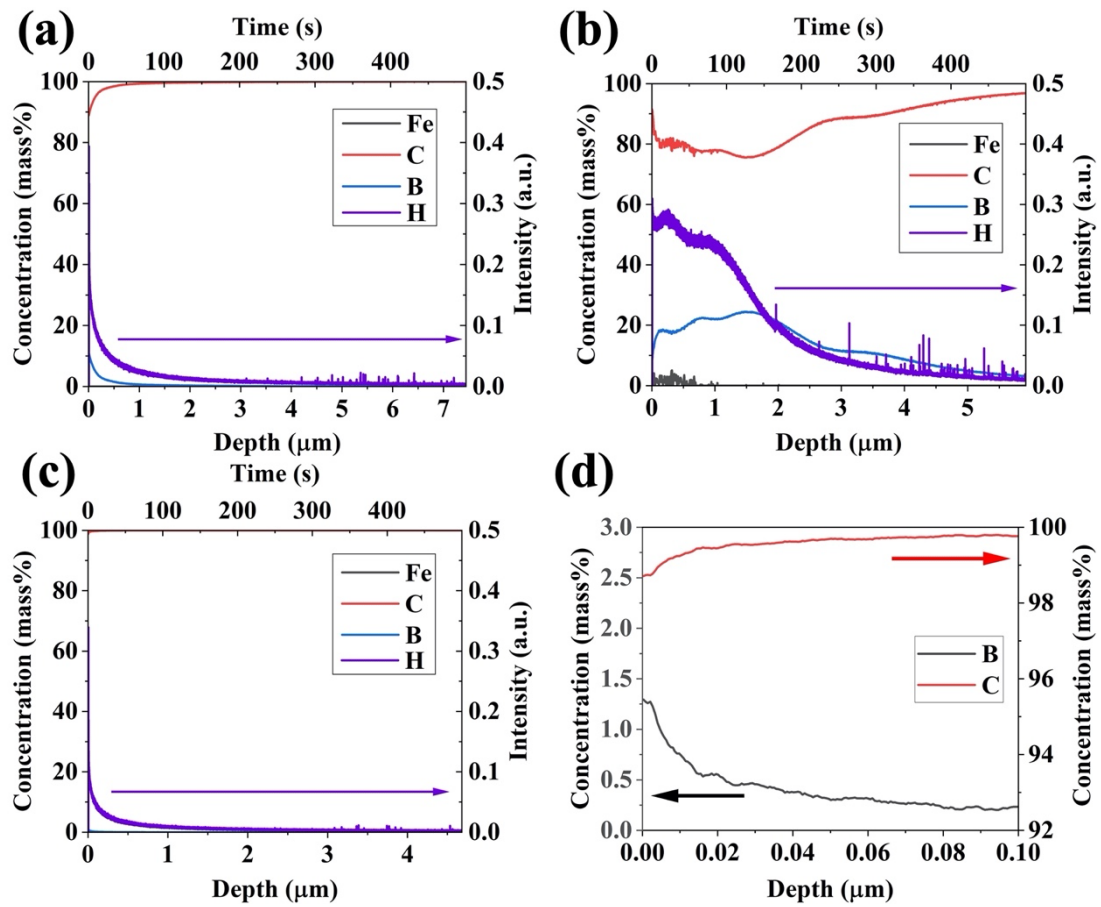


Fig. 4. Elements concentration as a function of depth as well as the H intensity as a function of sputtering time. (a), (b) and (c) are the results for the middle measurement spots on samples A-8, A-9 and A-20 from TDUs31-TM4h4, respectively. Fig. (d) is an enlargement of Fig. (c).

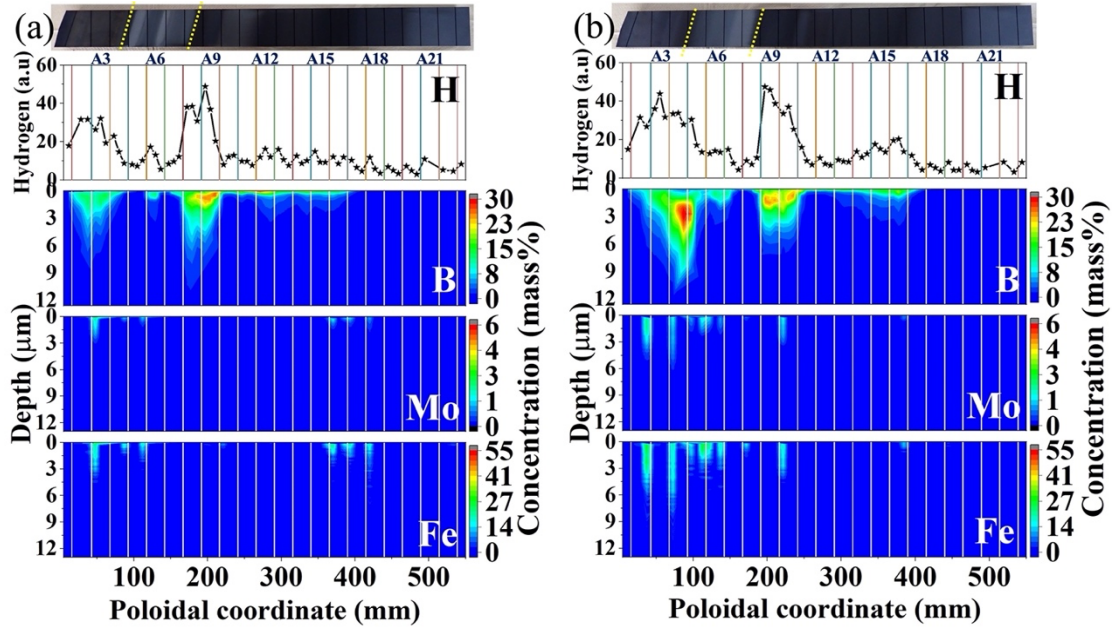


Fig. 5. Photo of target element, H retention, as well as depth resolved distribution patterns for B, Mo and Fe at TDUs3-TM4h4. (a) TDUs3u-TM4h4 and (b) TDUs3l-TM4h4.

The depth resolved impurity deposition patterns on TDUs3-TM3v5 are shown in Fig. 6(a) and (b). A wide B deposition region ($s = 30-221$ mm) is observed on the TDUs3-TM3v5. The B deposition thickness on the TDUs3u-TM3v5 is larger than that on the TDUs3l-TM3v5. Both horizontal and vertical target elements results show that the B deposition region has higher H retention due to the co-deposition with deposits. The Fe and Mo distributions are approximately consistent with the B distribution that mainly exist in the deposition dominant regions. As shown in Fig. 5 and 6, the distribution pattern of Fe and Mo are discretized. And the depths of Fe and Mo are smaller than that of B deposition. Because no glow discharge conditioning (GDC) was carried out after boronizations and excessive hydrogen and helium GDC was carried out in OP 1.2a. If GDC was the reason for the discretized Fe and Mo deposition peaks, larger depositions should be seen at larger depth. During OP 1.2b, two steel components melting events were observed [1,16]. These results show that the discretized deposition peaks of Fe and Mo are quite likely occurred during OP

1.2b. In addition, Mo from the marker layers on the divertor targets also contribute to the Mo deposition.

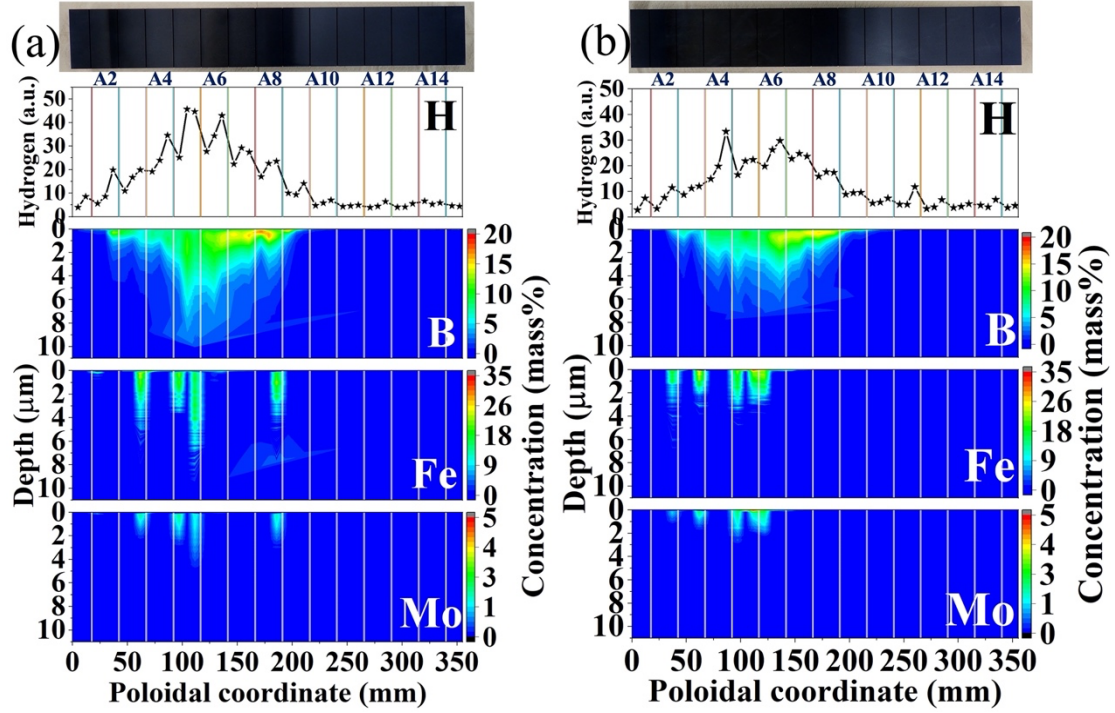


Fig. 6. Photos of target element, H retention, as well as depth resolved distribution patterns for B, Fe and Mo at TDUs3-TM3v5. (a) TDUs3u-TM3v5. (b) TDUs3l-TM3v5.

3.3 Up-down asymmetries in B deposition

Amount of deposited B on each GDOES measurement spot is plotted as a function of poloidal coordinate as shown in Fig. 7(a) and (d). Up-down asymmetries in B deposition location and amount exist on the TDUs3-TM4h4 and TDUs3-TM3v5. The difference of deposited B distribution patterns on the s-coordination between TDUs3u-TM4h4 and TDUs3l-TM4h4 is ~3 cm. The B deposition pattern on the TDUs3u-TM4h4 is closer to the PG than that on the TDUs3l-TM4h4. The total deposited B, Fe and Mo weight on the target elements, which are a sum of all of the GDOES measurement spots, are summarized in Table 2. The B, Fe, and Mo deposition amount on TDUs3u-TM4h4 are smaller than that on TDUs3l-TM4h4. The difference in B deposition amount on TDUs3l-TM4h4 and TDUs3u-TM4h4 is mainly

caused by the difference in B deposition region closed to PG, as shown in Fig. 7(a). Unlike to the horizontal target elements, the B deposition region on TDUs3u-TM3v5 and TDUs3l-TM3v5 are similar with each other except that the peak on the TDUs3u-TM3v5 is ~ 3 cm shifted to the PG side, as shown in Fig. 7(d). The total B, Fe and Mo deposition amount on TDUs3u-TM3v5 are larger than that on TDUs3l-TM3v5.

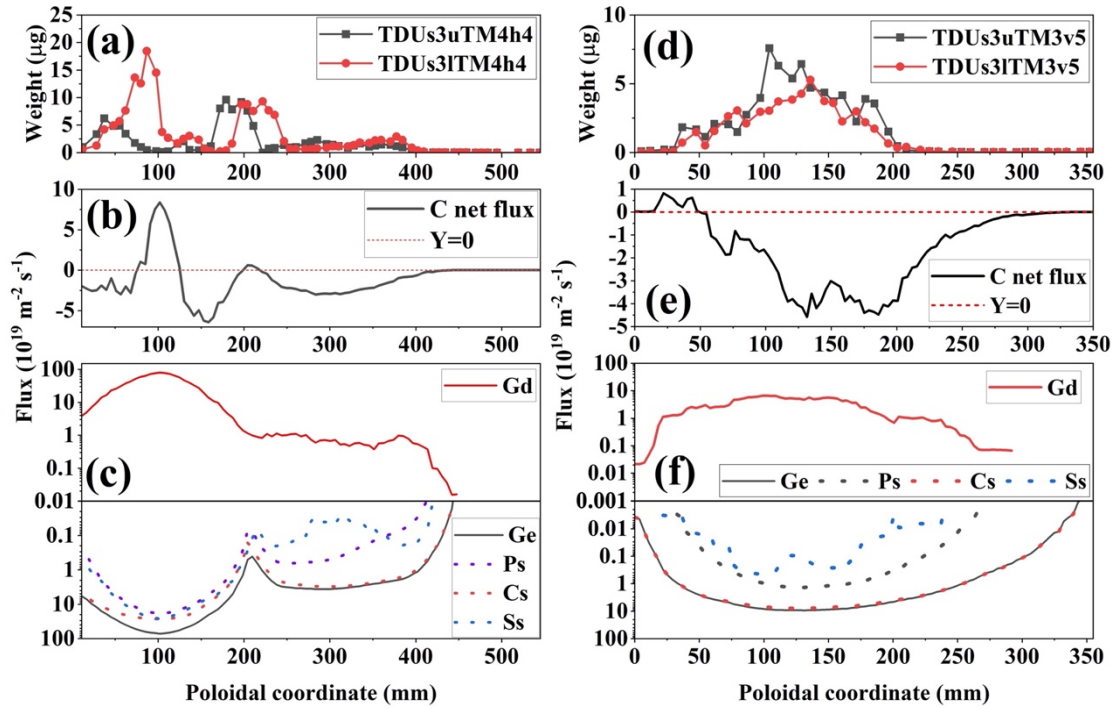


Fig. 7. Poloidal distribution of B deposition amount on TDUs3u-TM4h4 and TDUs3l-TM4h4 (a), TDUs3u-TM3v5 and TDUs3l-TM3v5 (d). ERO2.0 simulated net C flux on TM4h4 (b) and TM3v5 (e). The C deposition and erosion flux on TM4h4 (c) and TM3v5 (f) calculated by ERO2.0 where Gd, Ge, Ps, Cs and Ss, are the abbreviation of gross deposition, gross sputtering, chemical sputtering and self sputtering, respectively.

Table. 2. The total deposition amount of B, Fe and Mo measured by GDOES in unit μg .

Target element Element	TDUs3-TM4h4		TDU3s-TM3v5	
	upper	lower	upper	lower
B	108	180	73	54
Fe	32	68	38	22
Mo	1	4	2	1

3.4 Discussion

In-vessel material migration in W7-X has been numerically simulated by using ERO2.0 code [8]. Although B migration was not simulated at present, it is worth comparing the observed B deposition profiles and the simulated deposition/erosion profile of C because they have similar mass. The C erosion and deposition profiles on the TM4h4 and TM3v5 under standard magnetic configuration were calculated using ERO2.0 code. The standard magnetic configuration is the most used discharge configuration in OP 1.2 and takes a percentage of 57% in all the discharge time of the four magnetic configurations. The plasma background under standard configuration, an upstream density of $4 \times 10^{19} \text{ m}^{-3}$, an input power of 4 MW, a radiated power fraction of 33%, a downstream peak power flux of 1 MW m^{-2} at the strike line, from EMC3-EIRENE [19] were used as input parameters for ERO2.0 [9]. The calculated distribution patterns of net C flux, which is obtained by the gross deposition flux minus gross erosion flux, on the TM4h4 and the TM3v5 are shown in Fig. 7(b) and (e). The positive and negative values of net C flux correspond to the deposition and erosion of C, respectively. The gross C deposition fluxes (red line), the C gross erosion flux (black line), as well as the physical sputtering and chemical sputtering fluxes by impinging protons and charge exchange hydrogen atoms, self-sputtering flux on the TM4h4 and the TM3v5 are shown in Fig.7 (c) and (f). For the net C flux on the TM4h4 shown in Fig. 7 (b), two net C deposition regions are shown at similar position with the experimentally observed two large B deposition regions shown in Fig. 7 (a). The net C flux in regions $s = 221\text{-}400 \text{ mm}$ on the TM4h4 and $s = 50\text{-}200$

mm on the TM3v5 calculated by ERO2.0 show C erosion dominant however B deposition is observed in these regions.

The above results show that the observed B deposition profiles correlate to the calculated C deposition/erosion profiles. Possibly, B migrated with plasma, and its deposition profiles on the horizontal and vertical target elements are similar to the C gross deposition profile as shown in Fig. 7. Deposited B was eroded by physical sputtering as the same as deposited C. Therefore, the B profile has two peaks at both sides of strike line region as the same as the C case, as shown in Fig. 7(a) and (b). But, the chemical sputtering of B is lower than that of C [20]. And B deposition layer remained at positions ($s = 221\text{-}400$ mm on the TM4h4 and $s = 50\text{-}200$ mm on the TM3v5) where physical sputtering is weak.

On the other hand, the B profile on target element is a combination results of different discharges. Discharges under the other configurations also contribute to the B deposition profile. Fig. 8 shows the power flux, which are measured by infrared cameras [20], on TDUs3-TM4h4 and TDUs3-TM3v5 under different discharge configuration. These discharges have around 4 MW no-radiative power. In Fig. 8(c) and (d), the data on TDUs3-TM3v5 beyond 220 mm is not shown because of strong reflections there. Also, power flux on TDUs3-TM3v5 under high iota and low iota configuration are not shown because of small heat loads there. The much high power flux on TDUs3u-TM3v5 under high mirror configuration is caused by the error fields and particle drifts. The discharge number and time for the power flux in Fig. 8 are summarized in Table. 3. As shown in Fig. 8(a) and (b), discharges under low iota configuration also contribute to the B deposition in regions $s = 221\text{-}400$ mm on the TDUs3u-TM4h4 and the TDUs31-TM4h4.

The up-down asymmetries in deposition layer formation are observed on the TDUs3-TM4h4 and TDUs3-TM3v5. The B, Fe and Mo deposition amount on TDUs3u-TM4h4 are smaller than that on TDUs31-TM4h4. This also is the case for the power flux on TDUs3-TM4h4, as shown in Fig. 8(a) and (b), that higher power load on TDUs31-TM4h4 than TDUs3u-TM4h4. In the case of the vertical target elements, the B, Fe and Mo deposition amount on TDUs3u-TM3v5 are larger than that on

TDUs31-TM3v5. The deposition regions on TDUs3u-TM3v5 and TDUs31-TM3v5 are consistent with each other, as shown in Fig. 7 (d). A difference of ~ 3 cm in peaks of B deposition on the s-coordinate is observed on TDUs3-TM4h4 and TDUs3-TM3v5. The B deposition peaks on the TDUs3u-TM4h4 and TDUs3u-TM3v5 are closer to the PG than that on the TDUs31-TM4h4 and TDUs31-TM3v5. These up-down asymmetries in B deposition are considered mainly to be caused by the edge particle drift. Although, the upper and lower divertor targets are identical in their geometry and in the topology of magnetic field, movements of charged particles can be drifted by magnetic field (\mathbf{B}), electrical fields (\mathbf{E}), the curvature, and gradients of magnetic field strength [21–23]. In W7-X, the intersection of scrapper-off layer (SOL) flux tubes and divertor target forms the SOL region on divertor target. On the side of SOL region close to PG is the shadow region which is caused by the discontinuous nature of the W7-X target. The other side of SOL region is the private flux (PF) region, see Fig. 5 in Ref. [12]. The edge particle drift effects on the up-down asymmetries in heat and particle fluxes were studied by comparing similar plasma discharges conducted with reversed magnetic field under lower iota configuration in Ref. [12]. The results illustrated that the radial electrical field (\mathbf{E}_r) can lead to the difference in strike line location up to 3 cm in low plasma density discharge case. Furthermore, up-down asymmetry in heat flux at shadow region was also illustrated to be caused by the $\mathbf{E}_r \times \mathbf{B}$ drift. Although, the B deposition on horizontal target elements is mainly a PSI result under standard divertor configuration, as shown in Fig. 7. The standard and low iota divertor configurations have analogous topological features that shadow region, SOL region and PF region. As shown in Fig.7 (a), two large B deposition regions closer and farther to PG may correspond to the shadow region and PF region, respectively. Therefore, the up-down asymmetries in B deposition on TDUs3-TM4h4 is also considered to be caused by the $\mathbf{E}_r \times \mathbf{B}$ drift. As shown in Fig. 8(c) and (d), the up-down asymmetry in B deposition amount on TDUs3-TM3v5 could be a combination result of the particle drift and error fields.

The normal magnetic field direction, which is also the most used magnetic field direction, is counter clockwise when viewed from the above of W7-X. Meanwhile,

the discharges shown in Fig. 8 are all conducted under the normal magnetic configuration. Thus, the up-down asymmetries in deposition location and amount shown in section 3.3 will occur under the normal magnetic direction of W7-X. Due to the existence of up-down asymmetries in deposition, the strike zone will move to the deposition dominant region when the magnetic field direction is reversed. As the deposition layer has high H retention and difference mechanical property with the base material, reverse magnetic field will then give rise to H release and dust formation. This indicates that the up-down asymmetries in impurity transport and deposition need to be considered in the operation of W7-X. And the experimentally measured impurity distribution on target elements shown in this paper can be a benchmark for the simulation on the impurity transport in W7-X stellarator.

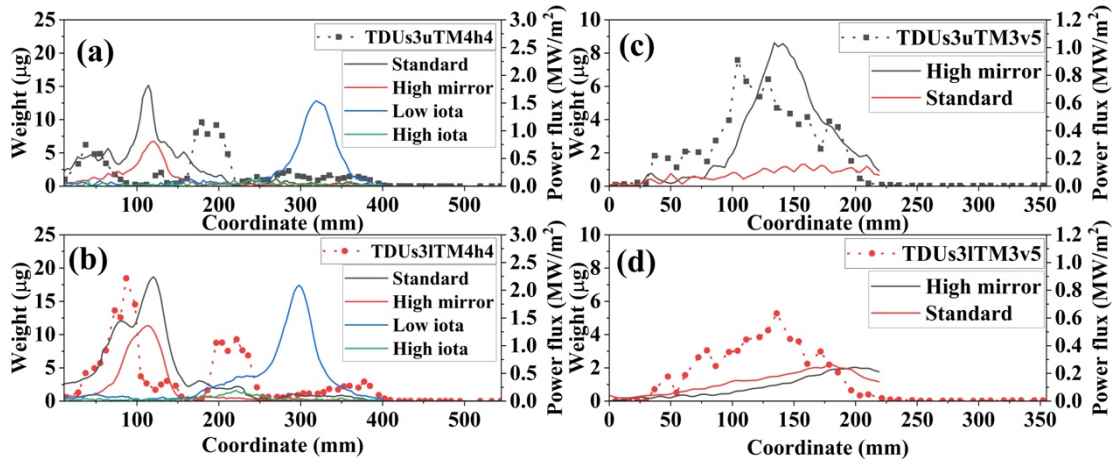


Fig. 8. The B profiles and heat flux under various configurations on the TDU3u-TM4h4 (a), TDU31-TM4h4 (b), TDU3u-TM3v5 (c), and the TDU31-TM3v5 (d).

Table. 3. The discharge number and time for the power flux used in Fig. 8.

TDUs3-TM4h4/TM3v5	Number	Time
Standard	2018/09/20-018	2 s
High mirror	2018/08/23-043	4.4 s
Low iota	2018/08/29-009	1 s
High iota	2018/09/12-023	2s

4. Conclusion

The impurities deposition on upper and lower target elements TM4h4 and TM3v5 from TDUs3 of W7-X was analyzed by TEM and EDS combined with FIB as well as GDOES. The EDS results show the existence of stainless steel composition in deposition layer. The depth resolved deposits distribution patterns and H retention on upper and lower TDUs3-TM4h4 and TDUs3-TM3v5 were clarified by GDOES. The deposition dominant regions exhibit higher H retention than the erosion and low PSI regions. Results of comparison of the observed B profiles and the ERO2.0 calculated C erosion/deposition profiles suggest that B migrated with plasma and deposited with similar profiles as the C gross deposition profiles, and was eroded by physical sputtering. A difference between B and C is chemical sputtering. Because of the chemical sputtering of B is lower than that of C, the observed B deposition profile and the net C profiles are different. Up-down asymmetries in B deposition exist on TDUs3u-TM4h4, TDUs3l-TM4h4 and TDUs3u-TM3v5, TDUs3l-TM3v5 even though they are at the magnetically symmetric up-down position. The B deposition peaks on the TDUs3u-TM4h4 and TDUs3u-TM3v5 are around 3 cm closer to PG compared to that on the TDUs3l-TM4h4 and TDUs3l-TM3v5. The B deposition amount on TDUs3u-TM4h4 is lower than that on TDUs3l-TM4h4. In the case of

vertical target elements, B deposition amount on TDUs3u-TM3v5 is higher than that on TDUs3l-TM3v5. These up-down asymmetries in B deposition location and amount on target elements are mainly caused by the particle drift and error fields.

Acknowledgment

This work is supported by the NIFS Stellarator-Heliotron Association Committee (URSX209) and by a JSPS KAKENHI grant (18H01203). This work has been carried out within the framework of the EUROfusion Consortium, funded by the European Union via the Euratom Research and Training Programme (Grant Agreement No 101052200 — EUROfusion). Views and opinions expressed are however those of the author(s) only and do not necessarily reflect those of the European Union or the European Commission. Neither the European Union nor the European Commission can be held responsible for them.

Reference

- [1] C.P. Dhard, S. Äkäslompolo, M. Balden, J. Baldzuhn, C. Biedermann, T. Bräuer, S. Brezinsek, M. Endler, Y. Hayashi, D. Hwangbo, Inspection of W7-X plasma-facing components after the operation phase OP1. 2b: observations and first assessments, *Phys. Scr.* T171 (2020) 014033.
- [2] Y. Gao, M.W. Jakubowski, P. Drewelow, F. Pisano, A.P. Sitjes, H. Niemann, A. Ali, B. Cannas, Methods for quantitative study of divertor heat loads on W7-X, *Nucl. Fusion.* 59 (2019) 066007.
- [3] G. Motojima, S. Masuzaki, C.P. Dhard, M. Krause, D. Naujoks, Y. Hayashi, S. Brezinsek, In-vessel colorimetry of Wendelstein 7-X first wall components: variation of layer deposition distribution in OP1. 2a and OP1. 2b, *Phys. Scr.* T171 (2020) 014054.
- [4] M. Mayer, M. Balden, S. Brezinsek, V. V Burwitz, C.P. Dhard, A. Dudek, G. Ehrke, Y. Gao, H. Greuner, R. Guimarães, Material erosion and deposition on the divertor of W7-X, *Phys. Scr.* T171 (2020) 014035.
- [5] D. Zhao, R. Yi, J. Oelmann, S. Brezinsek, M. Rasinski, Y. Gao, M. Mayer, C.P. Dhard, M. Krause, Ex situ analysis of W7-X divertor plasma-facing components by picosecond laser diagnostics, *Phys. Scr.* T171 (2020) 014018.
- [6] D. Zhao, R. Yi, A. Eksaeva, J. Oelmann, S. Brezinsek, G. Sergienko, M. Rasinski, Y. Gao, M. Mayer, C.P. Dhard, Quantification of erosion pattern using picosecond-LIBS on a vertical divertor target element exposed in W7-X, *Nucl. Fusion.* 61 (2020) 016025.
- [7] R. Yi, D. Zhao, J. Oelmann, S. Brezinsek, M. Rasinski, M. Mayer, C.P. Dhard, D. Naujoks, L. Liu, J. Qu, 3-Dimensional analysis of layer structured samples with high depth resolution using picosecond laser-induced breakdown spectroscopy, *Appl. Surf. Sci.* 532 (2020) 147185.

- [8] T. Vuoriheimo, A. Hakola, J. Likonen, S. Brezinsek, T. Dittmar, M. Mayer, C.P. Dhard, D. Naujoks, F. Tuomisto, Deposition of ^{13}C tracer and impurity elements on the divertor of Wendelstein 7-X, *Phys. Scr.* 96 (2021) 124023.
- [9] S. Brezinsek, C.P. Dhard, M. Jakubowski, R. König, S. Masuzaki, M. Mayer, D. Naujoks, J. Romazanov, K. Schmid, O. Schmitz, Plasma-Surface Interaction in the stellarator W7-X: Conclusions drawn from operation with graphite Plasma-Facing Components, *Nucl. Fusion.* 62 (2022) 016006.
- [10] E. Wang, S. Brezinsek, S. Sereda, B. Buttenschön, T. Barbui, C.P. Dhard, M. Endler, O. Ford, E. Flom, K.C. Hammond, Impurity sources and fluxes in W7-X: from the plasma-facing components to the edge layer, *Phys. Scr.* T171 (2020) 014040.
- [11] R.C. Wolf, A. Alonso, S. Äkäslompolo, J. Baldzuhn, M. Beurskens, C.D. Beidler, C. Biedermann, H.-S. Bosch, S. Bozhnikov, R. Brakel, Performance of Wendelstein 7-X stellarator plasmas during the first divertor operation phase, *Phys. Plasmas.* 26 (2019) 082504.
- [12] K.C. Hammond, Y. Gao, M. Jakubowski, C. Killer, H. Niemann, L. Rudischhauser, A. Ali, T. Andreeva, B.D. Blackwell, K.-J. Brunner, Drift effects on W7-X divertor heat and particle fluxes, *Plasma Phys. Control. Fusion.* 61 (2019) 125001.
- [13] Y. Gao, Y. Feng, M.W. Jakubowski, J. Geiger, M. Endler, C.P. Dhard, C. Biedermann, D. Naujoks, T.S. Pedersen, R. König, Understanding baffle overloads observed in high-mirror configuration on Wendelstein 7-X, *Nucl. Fusion.* 60 (2020) 096012.
- [14] S. Sereda, S. Brezinsek, E. Wang, T. Barbui, R. Brakel, B. Buttenschön, A. Gorjaev, U. Hergenhan, U. Höfel, M. Jakubowski, Impact of boronizations on impurity sources and performance in Wendelstein 7-X, *Nucl. Fusion.* 60 (2020) 086007.
- [15] ISO 16962, Surface chemical analysis-Analysis of zinc- and/or aluminium-based metallic coatings by glow-discharge optical-emission spectrometry, (2005).

- [16] C.P. Dhard, S. Brezinsek, M. Mayer, D. Naujoks, S. Masuzaki, D. Zhao, R. Yi, J. Oelmann, K. Schmid, J. Romazanov, Plasma-wall interaction studies in W7-X: Main results from the recent divertor operations, *Phys. Scr.* 96 (2021) 124059.
- [17] R. Lunsford, C. Killer, A. Nagy, D.A. Gates, T. Klinger, A. Dinklage, G. Satheeswaran, G. Kocsis, S.A. Lazerson, F. Nespoli, Characterization of injection and confinement improvement through impurity induced profile modifications on the Wendelstein 7-X stellarator, *Phys. Plasmas.* 28 (2021) 082506.
- [18] T. Klinger, T. Andreeva, S. Bozhenkov, C. Brandt, R. Burhenn, B. Buttenschön, G. Fuchert, B. Geiger, O. Grulke, H.P. Laqua, Overview of first Wendelstein 7-X high-performance operation, *Nucl. Fusion.* 59 (2019) 112004.
- [19] F. Effenberg, H. Niemann, Y. Feng, J. Geiger, O. Schmitz, Y. Suzuki, A. Ali, T. Barbui, S. Brezinsek, H. Frerichs, Investigation of 3D effects on heat fluxes in performance-optimized island divertor configurations at Wendelstein 7-X, *Nucl. Mater. Energy.* 18 (2019) 262–267.
- [20] M. Jakubowski, P. Drewelow, J. Fellingner, A. Puig Sitjes, G. Wurden, A. Ali, C. Biedermann, B. Cannas, D. Chauvin, M. Gamradt, Infrared imaging systems for wall protection in the W7-X stellarator, *Rev. Sci. Instrum.* 89 (2018) 10E116.
- [21] P. Grigull, K. McCormick, Y. Feng, A. Werner, R. Brakel, H. Ehmler, F. Gadelmeier, D. Hartmann, D. Hildebrandt, R. Jaenicke, Influence of magnetic field configurations on divertor plasma parameters in the W7-AS stellarator, *J. Nucl. Mater.* 313-316 (2003) 1287–1291.
- [22] S. Masuzaki, H. Tanaka, M. Kobayashi, G. Kawamura, the LHD Experiment Group, Effects of drifts on divertor plasma transport in LHD, *Nucl. Mater. Energy.* 18 (2019) 281–284.
- [23] N. Asakura, ITPA SOL and Divertor Topical Group, Understanding the SOL flow in L-mode plasma on divertor tokamaks, and its influence on the plasma transport, *J. Nucl. Mater.* 363-365 (2007) 41–51.